DESIGN, MODELING AND CONTROL OF A MINIMALLY INVASIVE SURGICAL PLATFORM

BY

FANXIN WANG

THESIS

Submitted in partial fulfillment of the requirements
for the degree of Master of Science in Mechanical Engineering
in the Graduate College of the
University of Illinois at Urbana-Champaign, 2018

Urbana, Illinois

Adviser:

Professor Thenkurussi Kesavadas
Professor Placid M. Ferreira

ABSTRACT

Minimally invasive single-site surgery has been shown to reduce the invasiveness of surgery by requiring only one incision to access the abdominal cavity. However, this technique presents the surgeon with unique challenges and requires the development of new robotic platforms and surgical tools. To address these challenges, a 20 mm trocar is designed to guide the serial insertion and assembly of three individual 3D printed, 8 mm, 5+1 degree-of-freedom (DOF) manipulator tools and a standard 8 mm laparoscopic camera through a single port. Each dexterous manipulator is remotely driven by 12 actuation tendons and is composed of rigid links joined by hybrid flexure hinges. For ensuring large transition of the vision scope, a holding frame of the trocar is introduced. The holding frame consists 3 degree-of-freedom (DOF) rotating which enable a pivot point where the incision goes through, and one additional DOF that controls the incision depth. Haptic devices are applied for translating the dexterity of the human arm to both the internal operating field and the external positioning frame.

Keywords: single port, laparoscopic surgery, surgical robotic platform, haptic device

ACKNOWLEDGEMENTS

I would first like to thank my advisor Professor Thenkurussi Kesavadas of the University of Illinois Urbana-Champaign. The door to Prof. Kesh office was always open whenever I ran into a trouble spot or had a question about my research or writing. He consistently allowed this paper to be my own work, but steered me in the right the direction whenever he thought I needed it.

I would also like to thank my mother and father, Hongmei Wang and Guoxian Fan, their great support and believing give me force to accomplish this work. And I would like to thank my co-advisor Professor Placid M. Ferreira and my colleague Nicholas Toombs, for the constructive and innovative advice.

I would also like to thank all my laboratory colleagues, they have been helping and teaching me a lot during the whole project.

Dedication

To my parents, relatives, and friends

Contents

1. Introduction

1.1 Motivation

Minimally invasive robotic surgery has enabled surgeons to perform many complex procedures with more precision and flexibility than is possible using traditional laparoscopic methods. This work is to give flexible, low-cost, Single Port Minimally Invasive Robotic Surgical Platform. From the former work, a dual-manipulator SPLS system with its own robotic surgery digital simulator have been accomplished. This work aims specifically at providing the surgeon with a dexterous, light-size robotic surgical platform that maps the arm operating to the internal operating zone with minimal invasiveness.

1.2 Objectives

The primary objective for this research is to develop a comprehensive robotic surgery platform that consists of multiple serial inserted 6 degree of freedom tools and one 4 degree of freedom light-weight supporting frame. This objective was achieved by the following tasks:

1. Mechanical design, manufacturing and assembly of the supporting frame prototype. Including building the drives and electronic supports for the supporting frame.
2. Develop control algorithms for both manipulator tools and supporting frame, by modeling the kinematics and dynamics for both systems, improve the performance of the manipulator prototype by applying friction compensation.
3. Further developing the software for control and imaging system, providing an interface where manipulator tools' position is indicated correctly from encoders' feedback and surgeons can get training experience.

1.3 Outline

This thesis is divided into 9 chapters, the contents of which are stated as the following:

Chapter 2 contains a literature review, traditional laparoscopic surgery and robotic platforms that are previously constructed have been stated.

Chapter 3 contains a short description for the former design of the manipulator, and states the inverse kinematics and dynamics used in the control of the manipulator, and working space analysis for the manipulator tool

Chapter 4 contains a short description of the teleoperation scheme and showing the improvement in the performance of the manipulator prototype by applying friction compensation from the experimental results.

Chapter 5 contains a description for the design of the supporting frame, including the four-bar structure, fixed pivot point, and motor placement that minimizes the required driving torque. Also contains the drive module selection for the system

Chapter 6 contains the inverse kinematics and dynamics used in the control of the supporting frame, and contains the control scheme for the frame

Chapter 7 contains a description of the control algorithm for the supporting frame, including both gravity compensation in initializing the system and input signal tracking in surgery process, and contains a discussion of the experimental results of the supporting frame

Chapter 8 contains the conclusion of the research and suggestions for future work.

1.4 Contribution

In addition to tradition robotic SPLS surgery functionality, the work stated here would advance the adaptivity and lower the price for minimally invasive robotic systems, also smaller port would be introduced using this method. First, using the scheme we develop, both the size and weight for the whole system are reduced. For the first stage completed system, manipulators and supporting frame can be transported by a normal suitcase. Comparing to the Da Vinci surgical systems, our systems give better portability. And due to the innovative mechanical design of the supporting frame and insertion frame, we reduce the volume and weight of robot systems to a relatively low level that it can be fit in any space if there exists a surgical operating table, while ensuring both accuracy and precision.

2. Background

Laparoendoscopic single-site surgery (LESS) has been viewed as an important step for reducing the invasiveness of surgical procedures. Whereas traditional multiport laparoscopic surgery involves multiple incisions [1], The LESS technique is performed by inserting 2 to 3 curved laparoscopic tools through a single flexible port often located in a single incision made at the umbilicus [2]. The LESS technique should then, in theory, better for patients because it requires only one incision. However, LESS remains an unpopular technique due to the many challenges it presents to the surgeon. Traditionally, in LESS procedures, surgeons must coordinate the end-effector motion of rigid bent tools that are crossed at the point of incision. This causes an unnatural inverted hand-eye coordination and clashing where the tools cross. Robotic surgery platforms with increased manipulator dexterity should enabled surgeons to overcome this unnatural inverted motion and perform many complex procedures with more precision and flexibility than is possible using traditional LESS methods.

In recent years, several multi-port robotic platforms have been developed. Intuitive Surgical's Da Vinci [3] was approved by the Food and Drug Administration (FDA) in 2000 and remains the only commercially available robotic system for multi-port laparoscopic surgery. Da Vinci's success was due, in part, to the invention of a 3 DOF tendon-driven manipulator tool referred to as Endowrist®. Combined with the dexterity of the external robot arms, the Endowrist® gives the Da Vinci platform outstanding maneuverability with a total of 6 DOF at the tool tip. The Da Vinci platform can be retrofitted to be used in LESS procedures [4], however, due to the high cost, arm collisions and size, [5] the number of possible surgical procedures are limited.

Researchers have proposed single port robotic platforms with the aim of minimizing invasiveness and the recovery time for patients. Cheon et al. [6] constructed a single port robotic platform capable of a large workspace in the abdominal cavity. They made use of plate springs in place

of tendon-based actuation. This allowed greater applied forces at the end-effector. However, the actuator platform and port size are quite large. Dolghi et al. have developed a platform with two robotic arms with rigid links and a laparoscope called SISR [7]. They embedded small DC motors in the manipulator body at each joint. While this method does avoid complex tendon routing within the manipulator, additional complexity is introduced by replacing the cables with miniature motors, gears, and bearings. Manufacturing and assembly of these miniature components is also costly. The corresponding port size, reported as 30 mm, is also relatively large due to these additional components. Conrad et al. have developed Interleaved Continuum-Rigid Manipulation with a soft, flexible robotic manipulator [8]. They use flexible shafts to remotely drive cable motion in the manipulator. While the 1 DOF flexible continuum portion of the manipulator is small (6mm in diameter), the additional 2 DOF located in the proximal section is larger, and contains complex miniature gear transmissions. Ding et al. developed a single port robotic platform called IREP that allows for the insertion of two wire actuated snake-like robot arms and a laparoscope [9]. Titan Medical Inc. has also introduced a surgical system for minimally invasive abdominal surgical procedures called SPORT which is also a single port robotic platform. SPORT requires a 25 mm single-incision to insert two manipulators and a 3D laparoscopic camera [10].

3. Design and modeling for the manipulator tools

The former researchers have achieved development of robotic platforms for multiport access and single port access. However, it is shown from the literature that there is a need for robotic surgical platforms with a high dexterity, small port size below 25 mm for true single port procedures. Former researchers from this research group have designed 6 DOF tendon-driven robotic manipulator tool capable of tissue palpation and dissection. Moreover, a serial insertion of three 8 mm manipulator tools are developed for the 16 mm trocar.

3.1 Design overview

We have made two main mechanical design innovations. The first, and arguably, the most crucial design innovation is the insertion trocar. We have developed an 18mm trocar (shown in Figure 1) that is capable of delivering 3 manipulator tools and a scope to the operating field as shown in Figure 2b. The trocar and required incision can be kept small by inserting tools, through the trocar, in serial (one after the other) as opposed to in parallel as is done traditionally.

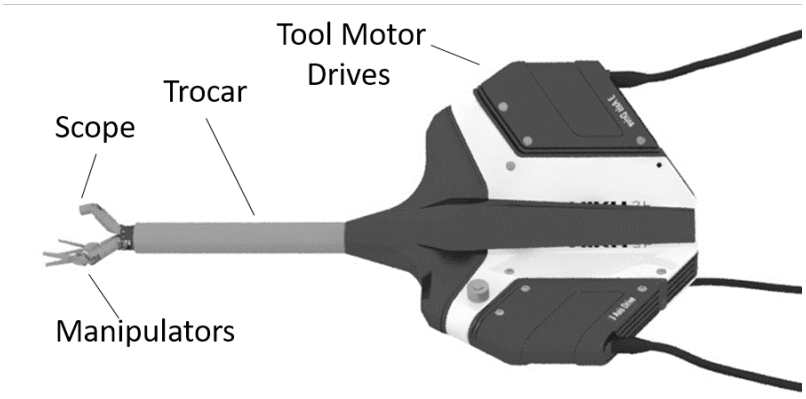

Figure 1) three tools (2 manipulators and scope) assembled in the custom trocar shown with the corresponding three motor drive units to the right (used to drive actuation cables).

The manipulator drive motors were moved to one side of the tool shaft Figure 2c-d and an additional hinge was added to the manipulator to enable this specific insertion method. The second major mechanical design innovation is the 5+1 degree-of-freedom manipulator. Because the tools are inserted and assembled adjacent to one another at the distal end of the trocar, the manipulator Figure 2a needs additional degrees of freedom to achieve the required triangulation necessary in surgery. These two major mechanical design innovations enable a minimally invasive robotic platform that is more flexible and compact when compared to other existing single and multi-port robotic platforms. We are planning to design and fabricate a trocar positioning arm Figure 2 b to position and orient the trocar in the vicinity of the incision.

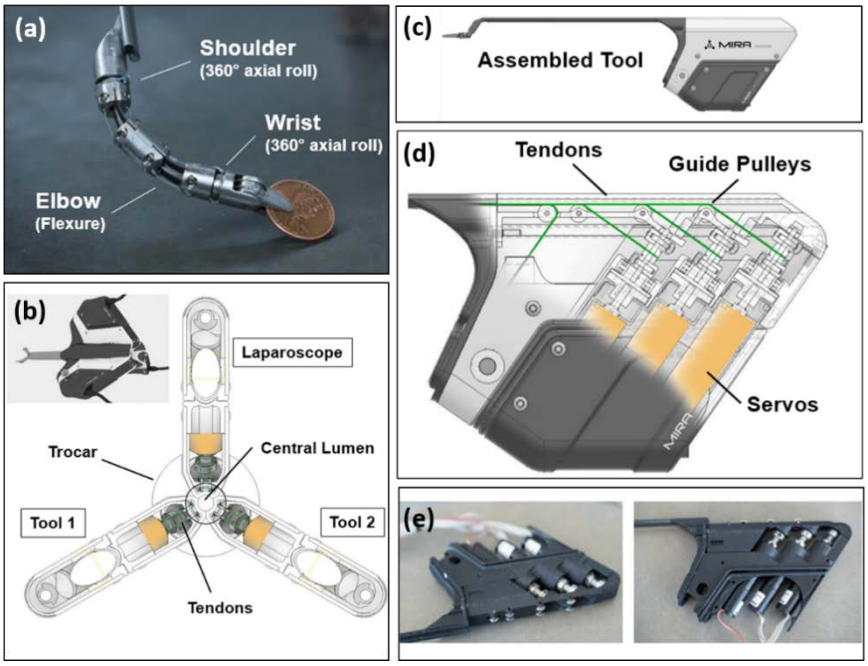

Figure 2) manipulator tool prototypes. (a) 5+1 degree of freedom stainless steel manipulator prototype, (b) axial cross-section of the three tools assembled in the custom trocar, (c) one full manipulator tool with manipulator at left, long cable guide tube and motor drives on the right, (d) cutaway of tool motor drive system and cables, (e) 3d printed tool with 12v gear motors, encoders and drive pulleys and cables.

3.2 Kinematics of the manipulator tool

The size of the port and the trocar are highly dependent on the size of manipulator body shown in Figure 3. Key elements including the roll and flexure joints and cable routing were designed to minimize the cross-sectional diameter of the manipulator while maximizing the dexterity and force output at the end-effector. The tendons were routed through a hollow core at the center of the manipulator to minimize joint coupling effects.

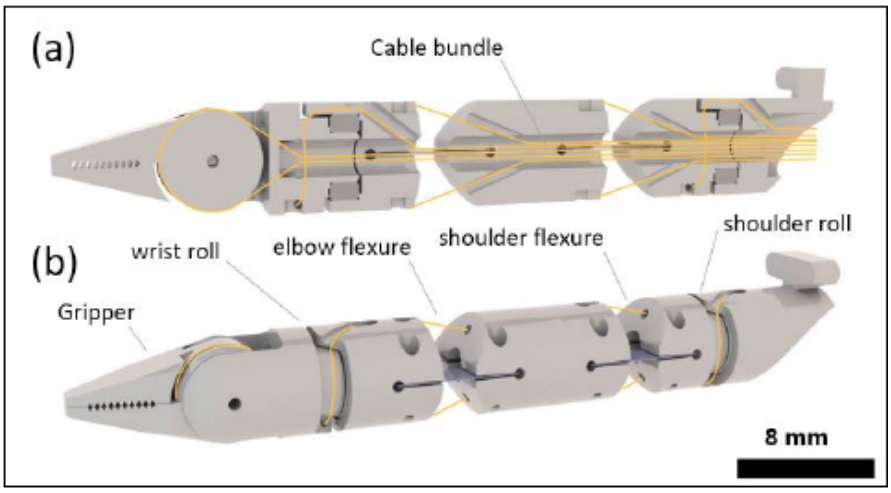

Figure 3) (a) cross-section of the manipulator showing the internal cable routing. (b) Two roll joints, two flexure joints and gripper direction provide 5+1 degrees of freedom

Figure 3 shows a schematic of one robot manipulator. 5+1 DOFs are $q1$, $q2$, $q3$, $q4$ and two independently controlled grippers' DOF $q5$ and $q5'$. The forward kinematics for the first three joints in the manipulator, the end-effector position which is the joint position of $q5$ in this case, can be calculated as:

$$\begin{bmatrix} x \\ y \\ z \end{bmatrix} = \begin{bmatrix} cos(q1) * (L3 * cos(q2 + q3) + L2 * cos(q2)) \\ sin(q1) * (L3 * cos(q2 + q3) + L2 * cos(q2)) \\ L1 + L3 * sin(q2 + q3) + L2 * sin(q2) \end{bmatrix}$$

where L1, L2, L3 are the link lengths between q1, q2; q2, q3; q3, q5 respectively. In this preliminary workspace analysis, we will neglect the action of the last two orientation DOF q4 and q5 and instead consider only the three positional DOF. Each of the flexure joints are limited to ±30° to ensure that the spring steel flexures remain in the elastic regime. Each roll joint is limited to ±180° to minimize twisting of tendons passing through the roll joints.

From the expression described above, it can be seen that a single manipulator end-effector position traces a spherical volume. In this analysis, we will consider the intersection of two manipulator workspace volumes as a valid cooperative workspace. We attempt to maximize this intersecting cooperative workspace region.

The inverse kinematics is needed for workspace analysis. The first three joints have the same layout as a 3 DOF articulated robot arm with inverse kinematics equation as:

$$\begin{bmatrix} q_1 \\ q_2 \\ q_3 \end{bmatrix} = \begin{bmatrix} \arctan 2(y, \mathrm{x}) \\ \arctan 2(y, \mathrm{x}) - \arctan 2\left(\sqrt{x^2 + y^2 - \left(L_2 \cos(q_3) + L_1\right)^2}, \mathrm{L}_2 \cos(q_3) + L_1 \right) \\ \arctan 2\left(\sqrt{1 - \dfrac{x^2 + y^2 - L_1^2 - L_2^2}{4L_1^2 L_2^2}}, \dfrac{x^2 + y^2 - L_1^2 - L_2^2}{2L_1 L_2} \right) \end{bmatrix}$$

3.3 Working space analysis

Researchers [6] claim that a workspace of 50x50x60 mm^3 is needed for common laparoscopic procedures. The frame supporting the trocar can vertically move the manipulators, the actual workspace requirements would be the maximum working plane larger than 50x50 mm^2. Two manipulators are required for laparoscopic procedures thus the intersecting volume of reachable space of the 2 manipulators should be maximized.

The longest continuous horizontal line inside the intersecting region is the diameter of largest circular plane in the working volume. In order maximum the workspace, the following equations can be derived geometrically as:

$$\begin{cases} \sqrt{(L_2+L_3)^2-(0.5d)^2}-L_4=h \\ \sqrt{(L_2+L_3+L_4)^2-h^2}=d+\sqrt{(L_2+L_3-L_4)^2-h^2} \\ x=2(0.5d+\sqrt{(L_2+L_3-L_4)^2-h^2}) \end{cases}$$

where L_4 is the length of gripper, d is distance between the first links of each manipulator, and x is the longest continuous horizontal line inside the cross section. We found that the cooperative workspace is maximized when d=12mm. The optimized working space is shown in Figure 4.

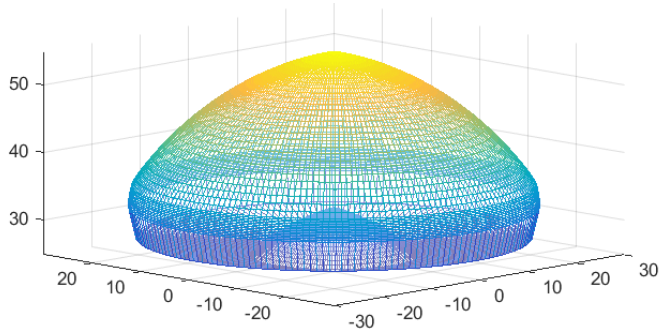

Figure 4 Optimized workspace result base distance 12mm (unit: mm)

3.4 Dynamic model of the manipulator tool

We formulated a dynamic model to better characterize the manipulator motion and tendon frictional effects. The equations of motion for the dual arm robot can be written in the following compact form:

$$M(q)\ddot{q}+C(q,\dot{q})\dot{q}+g(q)=S^Tu+J^T(q)F+S_0^Tr+f(T,q)$$

Note that $q \in R^5$ is the vector of generalized form of the 5 joint angles depicted in Figure 3, and $\dot{q} \in R^5$ is the corresponding vector of 5 joint angular velocity. $M(q) \in R^{5\times5}$ is the inertial matrix, $C(q,\dot{q}) \in R^{5\times5}$ is the centrifugal and Coriolis matrix, and $g(q) \in R^5$ is the vector of gravity forces. $S \in$

$R^{5\times5}$ is the joint selection matrix and $u \in R^5$ is vector of actuator torques, $S^T u$ represents the actuated joint toques. $J(q) \in R^{2k\times5}$ is the Jacobian which maps the generalized joint velocities to the linear and angular velocities of the end-effector. $F \in R^{2k\times5}$ is the vector of forces and torques applied on the end-effector. $J^T(q)F$ represents the outer forces and outer torques that applies on it. $S_0 \in R^{5\times5}$ is the selection matrix which selects out the flexural joints $q2$ and $q3$. $r \in R^5$ is the vector of reaction force of flexural joints $q2$ and $q3$. $S_0^T r$ represents the reaction force from bending the flexural joints. $f(T, q) \in R^{5\times1}$ is the vector of friction which is affected by the tension in the tendon-sheath actuation system used to drive the joint angles.

Euler-Lagrange equations can be used to derive the dynamics equations. For the 5-link robot described above, the linear and angular velocities of link i is expressed in terms of the Jacobian matrix and the derivative of the joint variables:

$$v_i = J_{vi}(q)\dot{q}, \omega_i = J_{\omega i}(q)\dot{q}$$

Then the kinetic energy of the manipulator is then given by

$$K = \frac{1}{2}\dot{q}^T \sum [m_i J_{vi}(q)^T J_{vi}(q) + J_{\omega i}(q)^T I_i J_{\omega i}(q)]\,\dot{q}$$

where m_i is the mass of link i, I_i is the inertia matrix of link i and is evaluated around a coordinate frame parallel to frame i with the origin located at the center of mass.

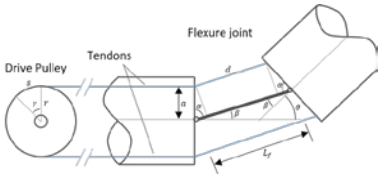

Figure 5 Simplified flexure joint kinematic model

In the case of rigid dynamics, the only source of potential energy is gravity. The potential energy can be computed by assuming that the mass of the entire object is concentrated at its center of mass and is given by:

$$P = \sum P_i = \sum g^T r_i m_i$$

where g is the vector giving the direction of gravity in the inertial frame and the vector r_i gives the coordinates of the center of mass of link i.

The Euler-Lagrange equations for a robotic system can then be stated as following:

$$L = K - P = \frac{1}{2}\dot{q}^T D(q)\dot{q} - P(q) = \frac{1}{2}\sum_{i,j} d_{ij}(q)\dot{q}_i\dot{q}_j - P(q)$$

$$\frac{d}{dt}\frac{\partial L}{\partial \dot{q}_i} - \frac{\partial L}{\partial q_i} = \tau_i$$

The overall Euler-Lagrange equations can be written:

$$\sum_j d_{kj}\ddot{q}_j + \sum_{i,j} c_{ijk}(q)\,\dot{q}_i\dot{q}_j + \phi_k(q) = \tau_k$$

where

$$c_{ijk}(q) = \frac{1}{2}\left\{\frac{\partial d_{kj}}{\partial q_i} + \frac{\partial d_{ki}}{\partial q_j} - \frac{\partial d_{ij}}{\partial q_k}\right\}, \phi_k(q) = \frac{\partial P(q)}{\partial q_k}$$

The Euler-Lagrange equations can also be written in matrix form as:

$$M(q)\ddot{q} + C(q,\dot{q})\dot{q} + g(q) = \tau$$

This dynamics model without the consideration of friction model is built.

4. Control algorithm for manipulator tools and experimental results

In order to achieve the goal of mapping the arm operating to the internal operating zone with minimal invasiveness, specific control schemes should be established. Different algorithms for controlling the manipulator tools are stated. Moreover, experimental results are presented to prove the effectiveness for the control algorithms.

4.1 Teleoperation scheme

An overview of the basic electronics layout used to control one 6 degree-of-freedom manipulator is shown in Figure 6.

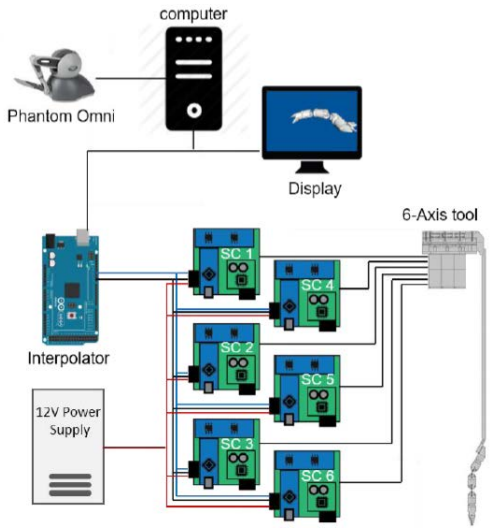

Figure 6 basic electronics layout of manipulator

Phantom Omni pen device are used to record the hand/arm movement from the operator. The movement information is then sent to the computer for computing the kinematics information. Then control signals are calculated in computer and sent to interpolator, which distributes to each of the 6 servo control cards to update each reference position. Each servo control board is connected to a Faulhaber 12V DC servo gearmotor to drive the manipulator.

4.2 Control scheme

The main idea of this control scheme is to choose the control effort u according to the equation so that the system is linear:

$$S^T u = M(q)a + C(q, \dot{q})\dot{q} + g(q) - (J^T(q)f + S_0^T r)$$

where a represents a new input to the system which needs to be selected. This means that for each joint k, a_k can be designed to control a scalar linear system. Moreover, if it is assumed that a_k is a function only of q_k and its derivatives, then a_k will affect q_k independently of the motion of the other links. Since a_k can be designed to control a linear second order system, a can be chosen as follows:

$$a = -K_0 q - K_1 \dot{q} + r_d$$

where K_0 and K_1 are diagonal matrices with diagonal elements consisting of position and velocity gains, so that the tracking error $e(t) = q - q_d$ satisfies the following equation:

$$\ddot{e(t)} + K_1 \dot{e(t)} + K_0 e(t) = 0$$

The overall system is close-looped and is globally decoupled, with each joint response equal to the response of a critically damped linear second order system.

The error for position tracking of the end-effector is less than 2%. We also see that error is not linear, which implies that source of the error is not linear with respect to angular displacement of the joints. The inverse dynamics control result for joint angular movement is shown in Figure 7. The percentage error for experimental joint angle tracking of inverse dynamics control is more than 5%.

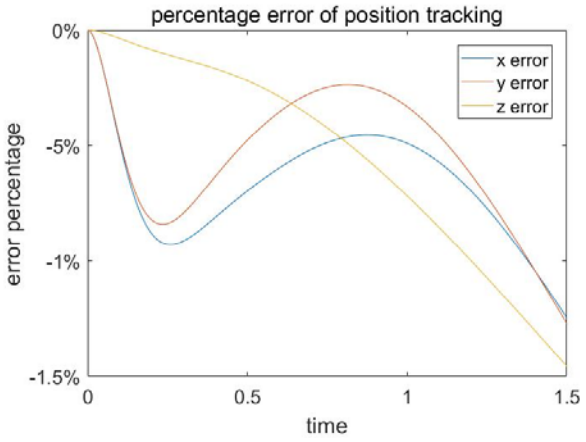

Figure 7 tracking error

4.3 Friction Model and friction compensation

Although the tendon-sheath remote actuation system has a low reasonably low coefficient of friction, we suspected that friction in the system would change depending on the bending or twisting of the joints. Tendon-sheath systems are also generally susceptible to backlash. Both of these phenomena can cause nonlinear motion of the tendon controlled joint. However, to minimize backlash in the system, a pretension was applied to all of the tendons. While this served to reduce backlash, it also increased normal forces which serve to further increase frictional forces. Therefore, we have chosen to model of friction here.

4.3.1 General infinitesimal element analysis for friction:

Considering the manipulator motion, the force is transmitted through tendon-sheath. When the tendon-sheath contacts with the manipulator metal surface, the normal force will introduce friction[11]. We use infinitesimal element analysis here to generate a general model for friction.

Assume that the angle between input tendon and output tendon is θ_p, as shown in Figure 8. Then the force equation along the radius:

$$\sum F_r = dF_r - (T + dT)sin\frac{d\theta}{2} - Tsin\frac{d\theta}{2} = 0$$

where, F_r is the reactional force on tendon-sheath along the radius direction, T is the pulling forces applied to the tendon-sheath. Assume that T varies little in the Infinitesimal. The dF_r can be derived:

$$dF_r = Td\theta$$

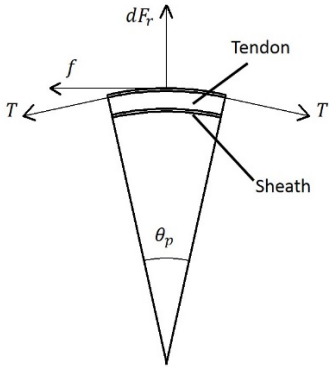

Figure 8 Infinitesimal element analysis of the cable

Denote the constant friction coefficient between the cable and sheath as f, the total friction force on a cable-sheath that has a span of θ_p is calculated as below:

$$f_a = f\int_0^{\theta_p} dF_r = \int_0^{\theta_p} fTd\theta = fT\theta_p$$

4.3.2 Roll joint contribution to friction

The first three DOF (shoulder roll joint, shoulder flexure joint and elbow flexure joint) fully define the position of end-effector in space and. For simplicity, the last 3 orientation DOF are neglected in this analysis. Due to tendon routing, the deflection of the first roll joint affects the friction in the tendon-sheath system actuating the second and third joints. Here we consider the extra 6 tendons used to control the 3 DOF of the gripper as static. These tendons form a bundle in the middle of the active tendons as shown in Figure 9a. There are 4 tendons outside the bundle that control the two flexure

joints. All of the tendons passing through the shoulder roll joint become twisted as the joint rotates through an angular displacement $q1$ as shown in Figure 9b.

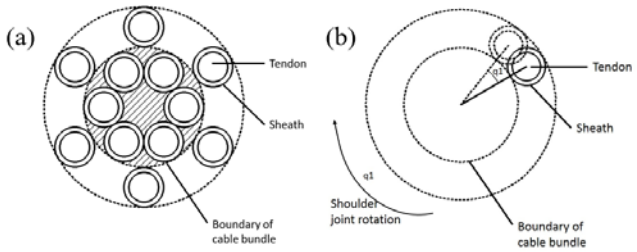

Figure 9(a) Sectional setting of cables inside a shoulder joint (b) Comparison of cables inside a shoulder joint for initial setting and after actuation

There are two components that need to be taken into consideration. The first is the friction term that affects all four tendons, actuating joint 2 and 3, equally. To simplify the problem, we consider one tendon transitioning from straight to a coiled configuration. The length of the contact line around the inner bundle is increased by the commanded angle $q1$. From the infinitesimal element analysis of the cable, derived previously, the friction is:

$$f_{q_i} = \int_0^{q_1} fT_{q_i} d\theta = fT_{q_i} q_1$$

where the T_{q_i} is the tension in tendons of joint i. And f_{q_i} denotes the friction on joint i occurring due to twisting in the roll joint.

The second aspect that cylinder-coiling configuration would affect is the tension inside outer cables. As the tendons twist around the inner bundle, they are stretched which produces additional tension in the tendon. For a cylinder with height h and radius R, and a commanded angular movement q_1 on shoulder roll joint, the increased tendon length is given as:

$$\Delta L = \frac{(q_1 R)^2}{h}$$

The tension increase due to coiling can be expressed as:

$$T_{ci} = \frac{\Delta L E \pi R^2}{l}$$

where E is the Elastic modulus of stainless steel and l is the total length of one cable.

So, for q_2 and q_3 in following derivation, the tension ${T_{q_i}}' = T_{q_i} + T_{ci}$.

4.3.3 Flexural joint contribution to friction

At each flexural joint, the tendon-sheath systems passing through the joint are also deflected by the commanded angle to that joint as shown in Figure 10.

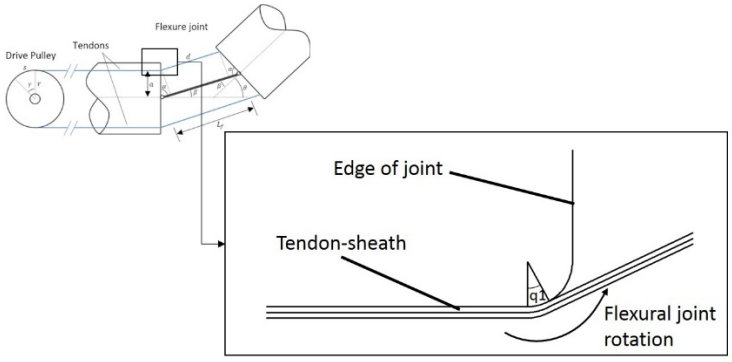

Figure 10 Friction in flexural joint

Using the same infinitesimal element analysis as before, we can derive the friction for cable of joint j inside joint i as:

$$f_{ij} = \int_0^{q_i} f {T_{qj}}' d\theta$$

4.3.4 Friction Simulation Results

To better understand the interaction between the two friction models discussed above, we performed a friction simulation by including these additional terms in the dynamics model.

The new friction terms are added to the force dynamics equations. Figure 11 shows the results of this friction simulation. In Figure 11a. we see that the friction forces grow to a maximum value of approximately 0.3 N for all joints as each reaches its maximum angular displacement of ±50 degrees. It can be seen that, as the first roll joint is actuated, the friction in the second and third joint increases nonlinearly. Figure 11b shows the change in friction seen by joint 3 as joint 2 is set to the +60 and -60 degree configurations.

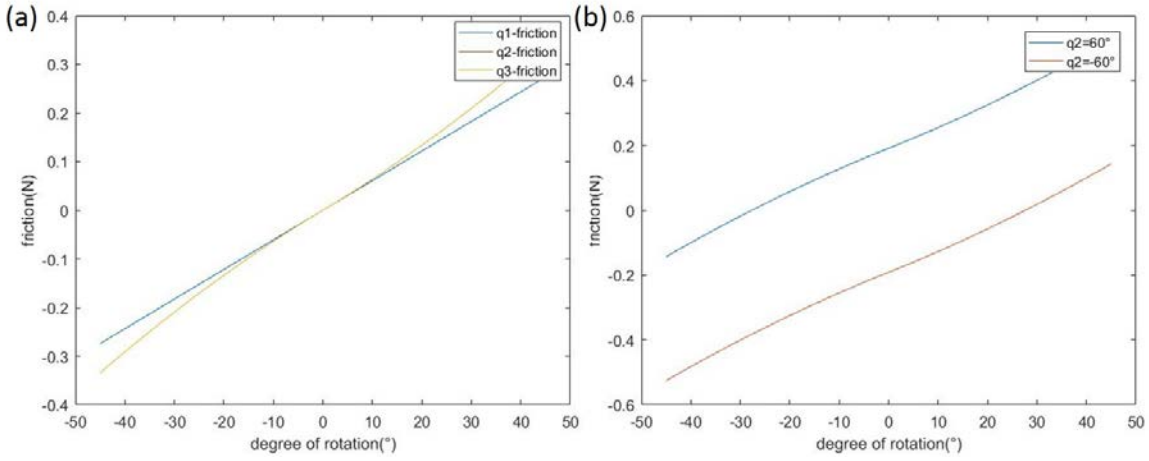

Figure 11 (a) Shows the friction in joints 1, 2, and, 3 (2 and 3 overlap) as they are independently actuated form -50 to +50 degrees. (b) Friction force on joints 3 as it is actuated from -50 to +50 degrees while joint 2 is set to -60 or +60 degrees configuration.

5. Design for the supporting frame

From chapter 3 and 4, a comprehensive prototype of the manipulator tool and the insertion trocar system has been stated. There is still a need to complete the design fabrication of a positioner arm to orient and stabilize the trocar in the vicinity of the incision. Thus far a motor-driven 3+1 degree-of-freedom arm (shown in Figure 12) to be attached to a standard operating table has been designed.

Figure 12 design overview

This design enables 3 axis of rotation: roll, pitch and yaw for the incision trocar and tools, and 1 translation on the depth control. Roll is achieved by belt transmission using DYN2 AC Servo Motor, pitch is achieved by gearbox transmission using DYN2 AC Servo Motor, yaw is achieved by directly driving the rotation on tool using Faulhaber Brushless DC-Servomotor. The additional depth control is achieved by Faulhaber Brushless DC-Servomotor driving a leadscrew to move the traveling block which is attached with whole trocar-assemble frame.

5.1 Design for the fixed pivot point for incision

For laparoscopic surgery, there will be incisions made on patients that allow tools to get through. For single port laparoscopic surgery (SPLS), it would be vital to keep the incision point fixed during the whole surgery procedure, for reducing the recovery time of patients and ensuring the safety during surgery. Thus, a fixed pivot point on the holding frame is needed for the trocar incision.

In order to achieve this functionality, a four bar structure is used for transmitting the torque. The simplified structure scheme is shown in the Figure 13, where length of bar 1 equals to bar 4, length of bar 3 equals to bar 2.

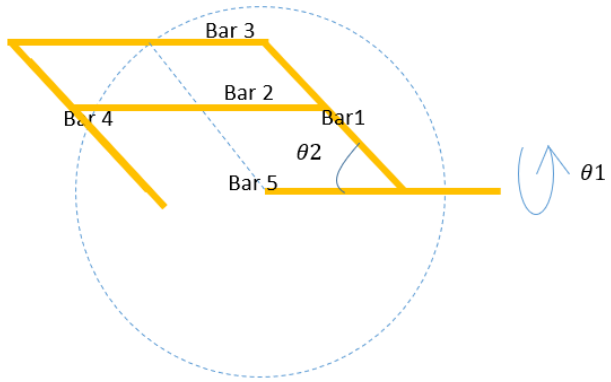

Figure 13 Simplified four bar structure

As bar 1 to bar 4 form a parallelogram 1, and as bar 1, bar 3, bar 4 and bar 5 form a parallelogram 2, the diagonal angles of the parallelograms are remained to be same. As the first degree of freedom θ_1 changes, though the parallelograms change into a different plane, the end of bar 4 which is the incision/pivot point remains in the same position in space. As the second degree of freedom θ_2 changes, as bar 5 is fixed, the second parallelogram has two fixed points that remain in the same position: the intersecting points of bar 1 and bar 5, and the intersecting points of bar 4 and bar 5. The latter one is also the end point of bar 4, which is the incision/pivot point. The last rotational degree of freedom is on bar 4 itself, which won't change the space position of bar 4. So far, if this structure is carried out in fabrication, then the end point of bar 4 will be the pivot point which allows a fixed incision.

5.2 Motor placement and selection

As the supporting frame is a motor-driven 3+1 degree-of-freedom arm, the last two degree of freedoms are yaw of the manipulator tool(which is the rotation on bar 4 itself) and the incision depth

control(which is the linear translation on bar 4). As the manipulator tool(bar 4) is light-weighted comparing to the 4 bar structure (bar 1, bar 2, bar 3, bar 5), the relative driving torque on degree 3 and degree 4 would be small. However, the driving torque for degree 1 and degree 2 would be large, which leading to large motors. In order to reduce the driving torque, a specified motor placing strategy should be carried out. We proposed the following transmission in Figure 14.

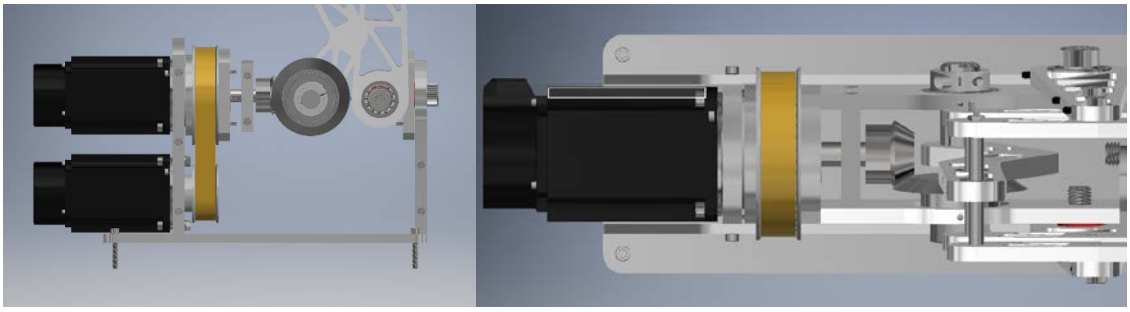

Figure 14 motor torque transmission.

The bottom motor is driving the first degree of freedom θ_1 using belt-gear transmission. The top motor is driving the second degree of freedom θ_2 using gear box of ratio 2:1. Using this certain structure, we are placing the motor 2 not only the linkage of bar 3, but on the bottom side, which reduces the weight and required torque for driving the system.

In order to reduce the complexity in building software and drive cards, minimal amount of motor types should be chosen. The required torque for different axis is calculated:

For axis 1 and axis 2:

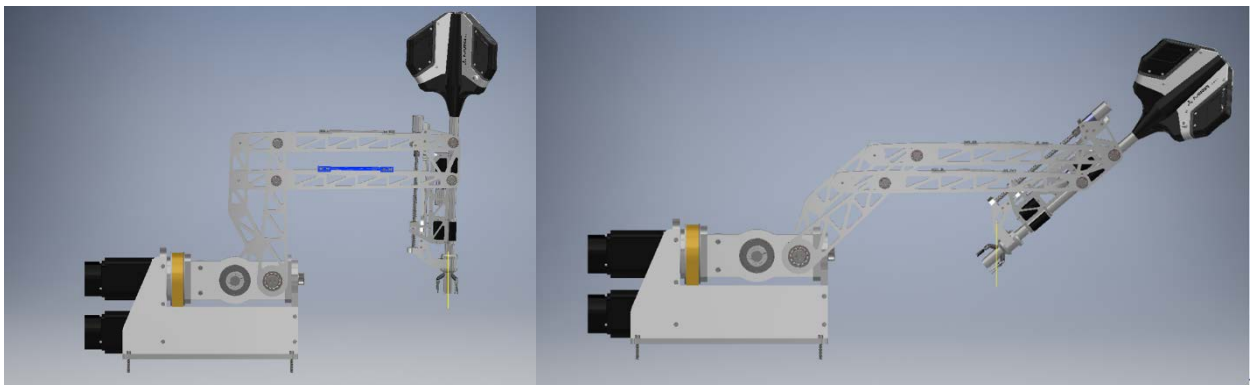

Figure 15 a. Max torque configuration for axis 1(roll) b. Max torque configuration for axis 2(pitch)

The maximum required torque is:

$$(m_{b2} + m_t)gl_{b2} + (m_{b1})gl_{b1} \approx 5Nm$$

where m_{bi} stands for mass of i-th bar, m_t stands for mass of the manipulator tool, g stands for gravity constant, l_{bi} stands for length of i-th bar.

DMM DYN2 series motor is chosen for first 2 axis:

Motor	**DMM DYN2**
Rated torque	3Nm
Frame size	86mm
Rated Speed	3000rpm
Gearbox ratio(needed)	2-10

Table 1: DMM DYN2 motor main parameter

As the axis 4(translation for insertion depth) has a lead screw for driving the tool, only axis 3(yaw) is taken into consideration:

$$T = m_t g * S/2\pi/effi \approx 0.02Nm$$

where m_t stands for mass of the manipulator tool, g stands for gravity constant, S stands for the

Since the frame size of the motor should be less then 30mm, Faulhaber Brushless DC-Servomotors series 3056b is picked for both axis 3 and axis 4:

Motor	Faulhaber Series 3056
Rated torque	0.03Nm
Frame size	30mm
Length	56 mm
Gearbox ratio(may need to slow rotation down)	/

Table 2: Faulhaber Brushless 3056b motor main parameter

6. Kinematics, dynamics and control scheme of the supporting frame

6.1 Kinematics, dynamics of the supporting frame

As described in Chapter 5, a specific structure for placing the motors that reduces the requiring torque is used. This will lead to a coupling in degree 1 and 2. The relation is shown in the following equation:

$$\begin{cases} \dfrac{M_1}{2} = \theta_1 \\ (M_2 - \dfrac{M_1}{2})/2 = \theta_2 \end{cases}$$

where θ_i stands for i-th degree of freedom rotation, M_i stands for i-th degree of freedom motor angular travel.

For simplicity, in the following equation and illustration, we will use the notation of θ_i(real rotation) instead of M_i(motor rotation).

Since the most heavy-duty parts are first 2 axis, it is vital to analysis the dynamics related to two AC servo motors. For modeling the system dynamics, we can regard the truss as bar with mass at the geometry center.

The mechanical modeling for the supporting frame is stated as following Figure 16 using truss replacement.

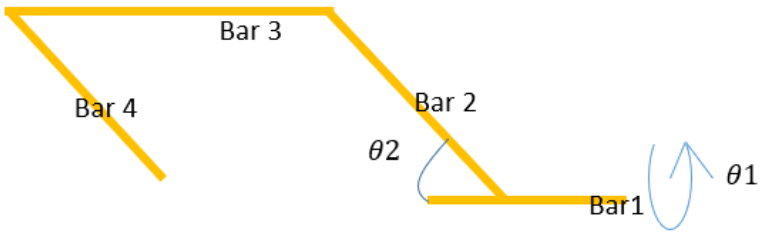

Figure 16 Modeling for supporting frame

where Length, mass, radius for each bar are denoted as lk, mk, rk, k=1,2,3. Angular travels for first and second axis are denoted as $\theta 1, \theta 2$.

As first and second axis are well decoupled, which means the dynamics functions are clear by calculating the required torque on each axis.

Axis 1:

$\tau_1 = \tau_{1d} + \tau_{1s} =$

$$\ddot{\theta_1}\left(\frac{m_1 r_1^2}{2} + \frac{m_2(r_2 sin\theta_2)^2}{4} + m_3(r_2 sin\theta_2)^2 + \frac{m_4(r_2 sin\theta_2)^2}{4}\right) + cos\theta_1\left(\frac{m_2 g r_2}{2} + m_3 g r_2 + \frac{m_4 g r_2}{2}\right)$$

Axis 2:

$\tau_2 = \tau_{2d} + \tau_{2s} =$

$$\ddot{\theta_2}\left(\frac{m_2 r_2^2}{4} + m_3 r_2^2 + \frac{m_3 r_3^2}{4} + \frac{m_4 r_2^2}{4} + m_4 r_3^2\right) + \frac{cos\theta_2 m_2 g r_2}{2} + m_3 g\left(r_2 cos\theta_2 + \frac{r_3}{2}\right) + m_4 g\left(r_2 cos\theta_2 + r_3 + \frac{r_2 cos\theta_2}{2}\right)$$

Using the same structure as stated in chapter 3, the equations of motion for the dual arm robot can be written in the following compact form:

$$M(q)\ddot{q} + C(q,\dot{q})\dot{q} + g(q) = \tau$$

Note that $M(q) \in R^{2\times 2}$ is the inertial matrix, $C(q,\dot{q}) \in R^{2\times 2}$ is the centrifugal and Coriolis matrix, and $g(q) \in R^2$ is the vector of gravity forces, $\tau \in R^2$ is the vector of motor torque.

6.2 Control scheme of the supporting frame

An overview of the basic electronics layout used to control the 3+1 degree of freedom supporting frame is shown in Figure 17.

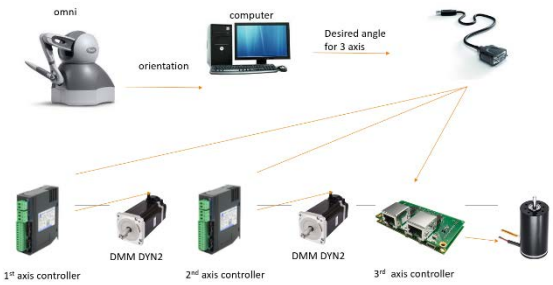

Figure 17 control scheme of supporting frame

Phantom Omni pen device are used to record the hand/arm movement from the operator. The movement information is then sent to the computer for computing the kinematics information. Then control signals are calculated in computer and directly sent to 4 servo control cards within serial port communication to update each motor reference position. After the supporting frame is set for proper surgery position, a switch to control the manipulator tools will be made to disable the control for supporting frame.

7. Control algorithm for supporting frame and experimental result

The main goal of this chapter is to develop control algorithm that satisfies the demand of trajectory tracking and gravity compensation. As the gravity compensation is specifically important in initialization for posing the surgical tool into a proper position, there is a mode selection in between the trajectory tracking and gravity compensation, so that the performance of initialization is certainly ensured.

7.1 Trajectory tracking

As the dynamic equation of the supporting frame is stated in chapter 6, the main idea of this control algorithm is to choose the control effort u according to the equation so that the system is linear:

$$S^T u = M(q)a + C(q,\dot{q})\dot{q} + g(q) - (J^T(q)f + S_0^T r)$$

where a represents a new input to the system which needs to be selected. This means that for each joint k, a_k can be designed to control a scalar linear system. Moreover, if it is assumed that a_k is a function only of q_k and its derivatives, then a_k will affect q_k independently of the motion of the other links. Since a_k can be designed to control a linear second order system, a can be chosen as follows:

$$a = -K_0 q - K_1 \dot{q} + r_d$$

where K_0 and K_1 are diagonal matrices with diagonal elements consisting of position and velocity gains, so that the tracking error $e(t) = q - q_d$ satisfies the following equation:

$$\ddot{e}(t) + K_1 \dot{e(t)} + K_0 e(t) = 0$$

The overall system is close-looped and is globally decoupled, with each joint response equal to the response of a critically damped linear second order system.

The corresponding result for tracking sine wave input is shown in Figure 18.

a

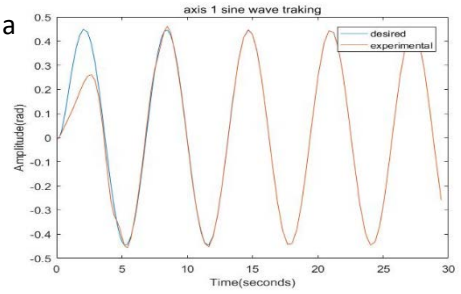

b

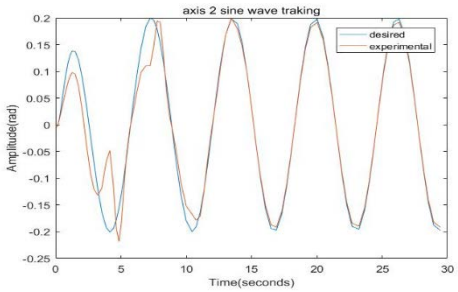

Figure 18 (a) axis 1 sine wave tracking (b) axis 2 sine wave tracking

The result shows that after certain period of time (in 10s), both axes achieve good tracking performance with an error rate less than 5%. The performance of axis 1 is smoother, while the performance of axis includes small perturbation in the starting phase, and cannot reach zero tracking error. This is generally caused by the backlash in the shaft coupling, as the backlash adds a delay whenever the trajectory changes direction, the control performance is limited.

7.2 Gravity Compensation

Despite the backlash in the direction changing, the dynamics and the structure is robust and with less uncertainty and disturbance, and the friction in the system is respectively low with bearings. Thus, the modelling for the system should be accurate enough to apply the model reference adaptive control (MRAC) algorithm.

A model-reference adaptive control (MRAC) system can be schematically represented by Figure 19. It is composed of four parts: a system containing unknown parameters, a reference model for specifying the desired output of the control system, a feedback control law containing adjustable parameters, and an adaptation mechanism for updating the adjustable parameters.

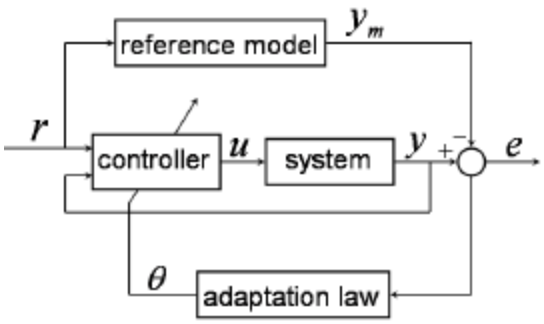

Figure 19 MRAC scheme

The reference model is used to specify the ideal response of the adaptive control system to the external command. It defines the ideal system behavior that the adaptation mechanism should seek in adjusting the parameters. The main point of this algorithm is to incorporate a reference model defining desired closed loop performance, adaptive laws are taken to adjust the controller parameters so that perfect tracking is asymptotically achieved.

MRAC will be used to reduce the nonlinearity of the system and track the linear reference model performance. Represent the system in the following form:

$$\dot{x} = Ax + W\varphi(x) + bu$$

where $x \in R^2$ is a vector of $\begin{bmatrix} \dot{q} \\ q \end{bmatrix}$, $A \in R^{2\times2}$ is a matrix that represents the linear part in the state space representation, $W\varphi(x) \in R^2$ is a vector that represents the nonlinear part in the system, $u \in R^2$ is a vector that represents input.

As the specific demand of gravity compensation, the required reference model should be high-damp second order system. Let the reference model be the following:

$$\dot{x}_m = A_m x_m + b_m r$$

where $x_m \in R^2$ is a vector of the state of the reference model, $A_m \in R^{2\times2}$ is a Hurwitz matrix, $r \in R^2$ is a vector that represents reference.

The direct adaptive reference feedback is defined as:

$$u = -\widehat{W}^T\varphi(x) - Kx + r$$

where $K \in R^{2\times2}$ is a chosen matrix such that,

$$A_m = A - BK$$

And the following adaptive law gives the estimate of the unknown parameters:

$$\dot{W} = -\Gamma\varphi(x)e^T PB$$

where Γ is the adaptive gain, $P = P^T > 0$ solves the algebraic Lyapunov equation for arbitrary $Q > 0$:

$$A_m^T P + PA = -Q$$

And e is the error between true state x and x_m.

Since the gravity compensation mainly used in the manual posing of supporting frame, the reference signal of the manual posing can be considered as step input signal. (while manual posing of the frame is hard to measure performance.)

The corresponding result for tracking step input is shown in Figure 20.

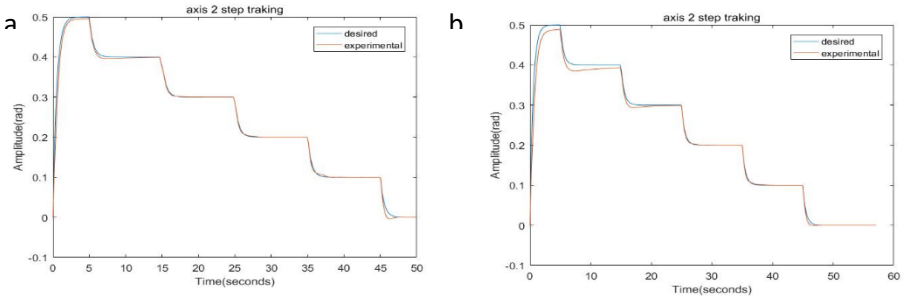

Figure 20 (a) axis 1 step tracking (b) axis 2 step tracking

The result shows that both axes achieve good tracking performance with an error rate less than 5%. The performance of axis 1 is more accurate, while the performance of axis has higher steady state error. This may also be caused by the backlash in the shaft coupling. But the overall gravity compensation is successful that manual posing of supporting frame is easily achieved.

8. Conclusion and future work

8.1 Conclusion

In this work a new solution for a robotic surgical platform including design and control of serial inserted manipulator tools are presented as well as the 3+1 DOF supporting frame has been completed. The proposed design differs from the previous robotic surgical platform presented in the literature since it does not involve the complexity in design and has an incision port size of 16 mm. Meanwhile, serial insertion of multiple tools is realized and 5+1 DOF manipulator tool are integrated on the robotic platform.

The innovative mechanical design of manipulator is discussed. For precisely commanding and controlling the manipulator tool, inverse dynamics control based on dynamic model is carried out. There is error when experiment is carried out, it is claimed that the most significant reason is friction. Thus, a nonlinear friction model is built, and friction compensation is carried out.

The light-weighted mechanical design of supporting frame is discussed. For precisely commanding and controlling the supporting frame, inverse dynamics control based on dynamic model is carried out. Also, gravity compensation worked out well for conveniently manual posing of supporting frame.

Software and control scheme are also well developed for this work.

8.2 Future work

We would like to improve the mechanical structure of the supporting frame as to have a better tracking performance. Currently the shaft coupling in second axis is causing backlash, which significantly limits the steady state error. A better way to figure out this design flaw should be carried out.

We would also integrate a new vision system that captures and transfers the inner sights to the surgeons. Introduce one additional tool which end-effector are consist of two micro fiber optics camera, enabling precise depth detection for clear manipulator-tissue interacting information. With the

embedded fiber optical camera, a vision-based sensing workflow will be developed for 3D tracking, pose estimation and scene reconstruction. As the proposed work been finished, the robotic surgical platform has multi tool insertion scheme and a high-fidelity imaging system, carrying out image-based AI analysis, improving surgical contact analysis via 3D reconstruction by providing haptic feedback geo feedback, and open up new surgery types which limits with small incision.

We would also try to examine our whole system performance. The validation on system will be testing our algorithms and mechanical robustness by creating silicon based phantom models (3D printed kidney for partial nephrectomy) and examine multi task on the model.

References

[1] R. Autorino, "Current Status and Future Directions of Robotic Single-Site," European Association of Urology, pp. 266-280, 2012.

[2] P. P. Rao, P. P. Rao and S. Bhagwat, "Single-incision laparoscopic surgery - current status and controversies," J Minim Access Surg, vol. 7, no. 1, pp. 6-16, 2011.

[3] G. S. Guthard and J. K. Salisbury, "The IntuitiveTM Telesurgery System: Overview and," in IEEE ICRA International Conferece on Robotics and Automation, San Francisco, 2000.

[4] M. Kroh, K. El-Hayek, S. Rosenblatt, B. Chand, P. Escobar, J. Kaouk and S. Chalikonda, "First human surgery with a novel single-port robotic system: Cholecystectomy using the da Vinci single-site platform," Surgical Endoscopy, vol. 25, no. 11, p. 3566–3573, 2011.

[5] M. Vargas, S. Cohen, T. Jackson, C. Hill-Lydecker and K. E. Ji, "Patient Perceptions of Robotic Surgery for Benign Gynecologic Disease," JOURNAL OF GYNECOLOGY RESEARCH, vol. 2, no. 1, 2016.

[6] B. Cheon, E. Gezgin, D. K. Ji, M. Tomikawa, M. Hashizume, H. J. Kim and J. Hong, "A single port laparoscopic surgery robot with high force transmission and a large workspace," Surgical Endoscopy, vol. 28, p. 2719–2729, 2014.

[7] O. Dolghi, K. W. Strabala and T. D. Wortman, "Miniature In Vivo Robot for Laparoendoscopic Single-Site Surgery," Surg Endosc, vol. 25, p. 3453–3458, 2011.

[8] B. L. Conrad and M. R. Zinn, "Interleaved Continuum-Rigid Manipulation: An Approach to Increase the Capability of Minimally Invasive Surgical Systems," IEEE/ASME Transactions on Mechatronics, vol. 22, no. 1, pp. 29-40, 2017.

[9] J. Ding, R. E. Goldman, K. Xu, P. K. Allen, D. L. Fowler and N. Simaan, "Design and Coordination Kinematics of an Insertable Robotic Effectors Platform for Single-Port Access Surgery," IEEE/ASME TRANSACTIONS ON MECHATRONICS, pp. 1-13, 2012.

[10] E. R. Raskin, "Evolution of Robotic Approaches for Colorectal Surgery," in Robotic Approaches to Colorectal Surgery, 2015, pp. 19-27.

[11] B. Cheon, E. Gezign, D. K. Ji, M. Tomikawa, M. Hashizume, H. J. Kim and J. Hong, "A single port laparoscopic surgery robot with high force transmission and a large workspace," Surgical Endoscopy, vol. 28, no. 9, p. 2719–2729, 2014.